


Single crystal diamond micro-disk resonators by focused ion beam milling ^F

Cite as: APL Photonics 3, 126101 (2018); <https://doi.org/10.1063/1.5051316>

Submitted: 07 August 2018 • Accepted: 25 September 2018 • Published Online: 15 October 2018

 Teodoro Graziosi, Sichen Mi, Marcell Kiss, et al.

COLLECTIONS

 This paper was selected as Featured



View Online



Export Citation



CrossMark

ARTICLES YOU MAY BE INTERESTED IN

Realizing $Q > 300\,000$ in diamond microdisks for optomechanics via etch optimization
APL Photonics 4, 016101 (2019); <https://doi.org/10.1063/1.5053122>

Design and focused ion beam fabrication of single crystal diamond nanobeam cavities
Journal of Vacuum Science & Technology B 29, 010601 (2011); <https://doi.org/10.1116/1.3520638>

Two-dimensional photonic crystal slab nanocavities on bulk single-crystal diamond
Applied Physics Letters 112, 141102 (2018); <https://doi.org/10.1063/1.5021349>

Learn more and submit

APL Photonics

Applications now open for the
Early Career Editorial Advisory Board

Single crystal diamond micro-disk resonators by focused ion beam milling

Teodoro Graziosi,^a Sichen Mi, Marcell Kiss, and Niels Quack^b
École Polytechnique Fédérale de Lausanne, 1015 Lausanne, Switzerland

(Received 7 August 2018; accepted 25 September 2018; published online 15 October 2018)

We report on single crystal diamond micro-disk resonators fabricated in bulk chemical vapor deposition diamond plates (3 mm × 3 mm × 0.15 mm) using a combination of deep reactive ion etching and Focused Ion Beam (FIB) milling. The resulting structures are micro-disks of few μm in diameter and less than 1 μm thick, supported by a square or diamond section pillar resulting from the multi-directional milling. Thin aluminum and chromium layers are used to ground the substrate, limit the ion implantation, and prevent edge rounding and roughening. FIB damage is then removed by a combination of hydrofluoric acid etching, oxygen plasma cleaning, and annealing at 500 °C for 4 h in air. We experimentally characterize the optical behavior of the devices by probing the transmission of a tapered fiber evanescently coupled to the micro-disk, revealing multiple resonances with a quality factor up to 5700 in the S- and C-band. © 2018 Author(s). All article content, except where otherwise noted, is licensed under a Creative Commons Attribution (CC BY) license (<http://creativecommons.org/licenses/by/4.0/>). <https://doi.org/10.1063/1.5051316>

I. INTRODUCTION

Single crystal diamond is an outstanding material with exceptional optical, mechanical, and chemical properties and thus an excellent candidate for integrated nanophotonics. The unique combination of optical material properties include an ultra-wide transparency window and low absorption from UV to IR, and the potential to integrate well-known color-center based emitters, such as nitrogen and silicon vacancy centers.^{1,2} Moreover, the high stiffness and low thermoelastic damping are particularly relevant for the fabrication of high frequency, low phase noise optomechanical oscillators. Recently, substantial advances have been reported in the development of diamond micro-nanofabrication processes, providing access to its excellent properties at the micro- and nanoscale, in particular, since high quality single crystal substrates have recently become readily available from several commercial suppliers. However, structuring of diamond is challenging due to the high chemical resistance, and the inability to grow or deposit single crystalline diamond thin films on substrates (such as silicon) further limits the possibilities compared to established material platforms like silicon or III-V compound semiconductors. In fact, for integrated photonics applications, it is important to have vertical confinement of light in waveguides and/or to suspend structures in order to sustain mechanical oscillations or displacements. Among the photonic devices that could benefit from a diamond platform, optomechanical oscillators are of particular interest, with applications in a wide range of domains,^{3,4} from fundamental building blocks to investigate quantum motion of solids,⁵ to demonstrate effects such as ground state cooling of the mechanical motion,^{6–8} quantum information processing,^{9–11} light squeezing,¹² and optomechanically induced transparency.^{8,13} In addition, optomechanical oscillators are of great interest for engineering applications, such as sensing (mass sensing,¹⁴ high bandwidth accelerometry,¹⁵ and displacement sensing¹⁶) and telecommunications (wavelength conversion,¹⁷ optical routing,¹⁸ light storage,¹⁹ and timing²⁰). In particular, diamond optomechanical oscillators can benefit from the low thermoelasticity, which can yield very high

^ateodoro.graziosi@epfl.ch

^bniels.quack@epfl.ch

mechanical quality factors (in excess of 1×10^6) even at room temperature.²¹ The mechanical quality factor describes the coupling of the mechanical oscillator with the environment, and its product with the oscillation frequency is useful as a figure of merit that gives an indication on the thermal decoherence, i.e., the temperature limit at which the optomechanical interaction can exist. To observe this interaction at room temperature, the Qf -product³ needs to be of the order of

$$Q_m f_m = k_B T / \hbar = 6 \times 10^{12}. \quad (1)$$

To reach this regime, a high mechanical frequency is desirable, in combination with a high mechanical quality factor. Micro-disks can offer a high mechanical frequency and mechanical quality factor with a relatively simple fabrication scheme.^{22,23} In the case of diamond, the micro-disk (and diamond waveguide) thickness has to be of the order of 300–400 nm to be a single-mode, a condition necessary to construct high-bandwidth integrated photonic circuits. For these thicknesses and micro-disk diameters of few micrometers, considering the diamond stiffness, the supported radial expansion mechanical oscillation mode (“breathing” mode) is in the 1-5 GHz range. This mode has high optomechanical coupling strength, and the mechanical frequency range is ideal for applications like frequency references in chip scale atomic clocks.²⁰

Few fabrication schemes have been proposed to create diamond photonic structures (Table I). We here present a fabrication method to structure freestanding microdisks and the corresponding support pillar using direct milling by Focused Ion Beam (FIB). FIB milling is a versatile fabrication approach to structure diamond, and it has been used not only to create suspended structures, like our micro-disk, but also for micro-optical components. Important examples are diamond solid immersion lenses (SIL), used to enhance the collection from diamond color-center emitters.^{24,25}

In the first five rows of Table I, we reported the literature results for diamond resonators fabricated using FIB for all or part of the processing. Our micro-disks can achieve higher optical quality factors. Typically, the main contribution to low Q-factors in FIB processed resonators is the FIB-induced damage, and in our work, we present a strategy to tackle the issue. In the table, the references shown report limited optical Q-factors (200)²⁶ or no optical cavity resonances^{29,33} for photonic crystal beam resonators. Other methods, not based on the use of focused ion beams, have been proposed, including thinning and patterning of a diamond slab transferred on top of a sacrificial substrate,²⁹ or modifying the incidence angles of reactive ions to achieve suspended structures with a triangular cross section (with a Faraday cage or by tilting and rotating the sample in a reactive ion beam Etcher).^{31,34,35} Micro-disk resonators have been fabricated in single crystal diamond using a “quasi-isotropic” undercut using high power oxygen plasma with no RIE platen bias, forming an octagonal section support pillar due to the crystal symmetry of the diamond lattice.^{32,36} With this method, optomechanical effects like optomechanically induced transparency were demonstrated,⁸ allowing creating additional suspended

TABLE I. Comparison with diamond resonators reported in the literature. The results presented in this work are marked by *. In the table, we compare the measured optical quality factor (Q_o) for the respective resonance wavelength (λ_0), resonator geometry, fabrication technique, and substrate used. Note that the probe wavelength and/or geometries are not of the same range for all the work presented here; in particular, resonators working at smaller wavelengths or based on photonic crystals may be more sensitive to fabrication defects.

References	Substrate	Resonator	Fabrication	λ_0 (nm)	Q_o
*	<i>Bulk CVD single crystal</i>	<i>Micro-disk</i>	<i>RIE, FIB</i>	1492	5 720
26	Bulk single crystal	Photonic crystal beam	FIB	627	221
27	Polycrystalline CVD thin film	Micro-disk	RIE, FIB sidewall smoothing	~1550	~100
28	Heteroepitaxial CVD membrane	1D and 2D photonic crystals	FIB on membrane	625	700
29	Bulk single crystal	Photonic crystal beam	RIE, FIB
	Single crystal membrane	Photonic crystal beam	RIE	567	1 710
30	Single crystal membrane	Photonic crystal beam	RIE	~660	24 000
31	Bulk CVD single crystal	Racetrack	Angled RIE	1648	151 000
		Photonic crystal beam	Angled RIE	1609	183 000
32	Bulk CVD single crystal	Micro-disk	Quasi-isotropic RIE etch	1540	335 000

structures such as photonic crystal membranes.³⁷ Direct FIB milling is the other option to fabricate suspended micro-disks. It allows us to have good control on the shape of the pillar, allowing to include structures like mechanical shields³⁸ or to fabricate any combination of disk diameter/pillar diameter, which is critical to achieve low substrate losses of the mechanical oscillation and thus a high mechanical quality factor.

In this contribution, we describe the fabrication scheme for single crystal diamond micro-disks, and we characterize the optical quality of the fabricated resonators. We report experimental characterization of the optical quality factor Q_O of single crystal diamond micro-disks fabricated by focused ion beam etching, representing an indirect measurement of the quality of the fabrication process and demonstrating the suitability of the process for the fabrication of optomechanical oscillators.

II. FABRICATION

The micro-disks were fabricated in a CVD single crystal diamond plate (3 mm × 3 mm × 150 μm, Lake Diamond). The diamond was coated with a 500 nm layer of sputtered SiO₂ (Pfeiffer SPIDER 600). We fabricated a recess in a silicon carrier wafer of the same dimensions of the diamond plate using direct writing lithography (Heidelberg MLA150) on a 0.6 μm layer of AZ ECI 3000 photoresist and transferring the design into the silicon wafer with Deep Reactive Ion Etching (DRIE). After stripping the photoresist, the diamond plate was positioned inside the recess in order to have the top face on the same level as the silicon wafer top surface, in order to enhance the spin coating uniformity and minimize edge beads. We coated the sample with a 0.6 μm layer of AZ ECI 3000 photoresist and used mask photolithography to expose the photoresist. The pattern was transferred into the SiO₂ hard mask first and the diamond later using DRIE (SPTS APS Dielectric Etcher). The plasma parameters used to etch the diamond are the same as used in Ref. 39 [2000 W inductively coupled plasma (ICP) power, 200 W bias power, 100 SCCM O₂, 15 mTorr chamber pressure]. The diamond was etched to obtain 12 μm tall cylindrical pillars. The plate was detached from the carrier wafer, the hard mask stripped in a bath of BHF, and the diamond coated with a 50 nm layer of sputtered Al and 75 nm of sputtered Cr (Alliance-Concept DP 650). We mounted the sample on a 45° holder and ground the top surface with conductive tape. The undercut is performed with a FEI Nova 600. The sample is milled from two directions to create a polygonal section pillar using 30 kV Ga⁺ ions with current ranging from 1 nA/cm² to 100 pA/cm². Higher ion current is used to remove most of the material. Similar to a typical TEM lamella fabrication procedure, we gradually reduce the ion current to achieve a better smoothness. By orienting the ion beam normal to the top surface of the diamond sample, we achieve additional smoothing of the micro-disk sidewall. The scheme of the FIB milling is shown in Figs. 1(7a)–1(7d). As we previously reported,⁴⁰ we deposit thin layers of aluminum and chromium to limit the gallium ion implantation and ground the top diamond surface. Chromium was chosen because it exhibits a good resistance to the Ga⁺ ions of the FIB, and aluminum was necessary to ensure good adhesion of Cr on diamond. Parts of the metal coating are milled to be able to access the diamond below, leading to an undesired gallium implantation of the exposed diamond areas. Nevertheless, the metal layer will prevent implantation into areas of the device that do not need to be etched by the ion beam but that are exposed during focusing and alignment. Figure 2 shows the implantation depth of 30 kV gallium ions in bare diamond and in diamond coated with the metal layers for different incidence angles, showing that the thickness of the implanted region is in the order of 10 nm, corresponding to the extension of the ion implantation profile of Fig. 2(a). The simulations of the penetration depth of the 30 kV gallium ions were performed with SRIM-2013.⁴¹ The metallic protective layers above the diamond also allow sharper sidewall angles. The Gaussian profile of the ion beam generates rounding of the features due to the extension of the ion tail outside the milling pattern, but the sacrificial layer, if resistant enough to the ion beam, absorbs the feature rounding and allows a sharp edge at the diamond interface. Given the slow etch rate of diamond, a very thick layer is needed to etch the several micrometers necessary to structure the pillar, while milling in the horizontal directions [Figs. 1(7b) and 1(7c)]. However, 50 nm of aluminum and 75 nm of chromium are sufficient to withstand the final smoothing step [Fig. 1(7d)], when only less than 1 μm of diamond needs to be milled. Additionally, the metal layer helps prevent the typical roughening of the sidewalls when FIB milling with the beam normal to the surface.⁴² During milling

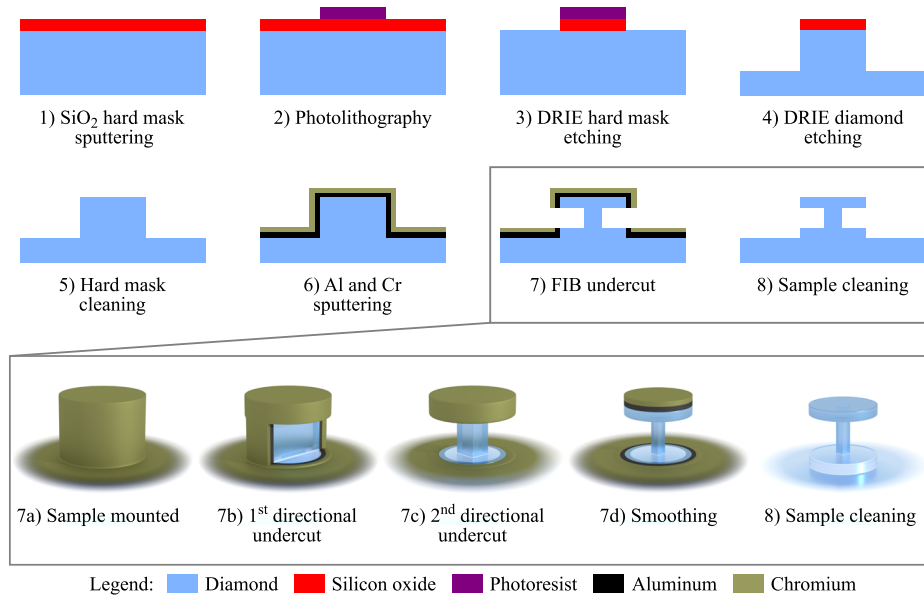


FIG. 1. Schematic of the process flow for the micro-disk fabrication. The diamond die is attached to a carrier wafer with a mounting wax, and the SiO₂ hard mask is sputtered (1). Optical lithography is used to pattern the photoresist, (2) and Deep Reactive Ion Etching (DRIE) is used to transfer the design first into the hard mask (3) and subsequently into the diamond substrate (4). After removing the hard mask (5), Al and Cr are sputtered (6), and the diamond is detached from the carrier wafer and processed with FIB [(7a)–(7d)]. Finally, the diamond is cleaned to remove the metal mask and the redeposited Ga/C layer and annealed to etch the FIB-induced damage layer (8). The inset shows the details of the FIB undercut protocol.

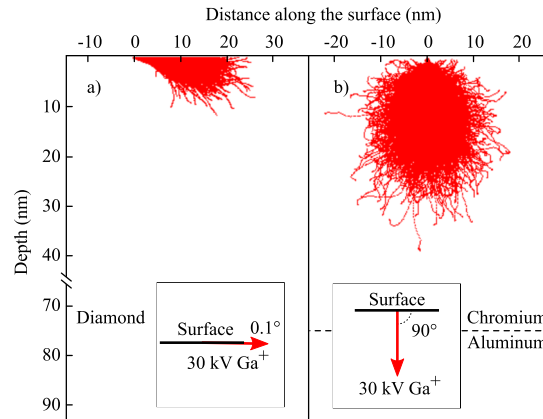


FIG. 2. Monte Carlo simulations of 30 kV gallium ions parallel (0.1°) to the diamond (a) and normal to the surface of the Cr/Al layer (b) surface. The chromium layer stops the Ga⁺ ions preventing implantation in the diamond lattice. When the diamond surface is exposed, the ion beam is always parallel to the exposed surface. The SRIM simulation shows that in this case, the depth of the implantation is of the order of ~10 nm.

with the FIB, part of the material is redeposited in proximity of the milled areas. It is expected that the deposit is composed mostly of amorphous carbon, gallium, and the masking metals (Al and Cr). The latter are easily removed by dedicated wet etchants, while amorphous carbon and gallium are very resistant to common oxidizer solutions, like piranha (H₂SO₄ 96%, H₂O₂ 30%, 3:1) or aqua regia (HCl 37%, HNO₃ 70%, H₂O, 3:1:2). Acid mixtures containing HClO₄ have been used to clean FIB fabricated diamond,^{26,28,43} however, we found that hydrofluoric acid, followed by microwave O₂ plasma (Tepla GiGAbatch barrel plasma stripper, 200 W, 200 SCCM O₂, 0.5 mbar), proved efficient in removing this redeposited layer. Finally, the sample is annealed in air at 500 °C for 4 h, heating the chamber at 50 °C/min, following similar procedure as in Ref. 44. As reported by

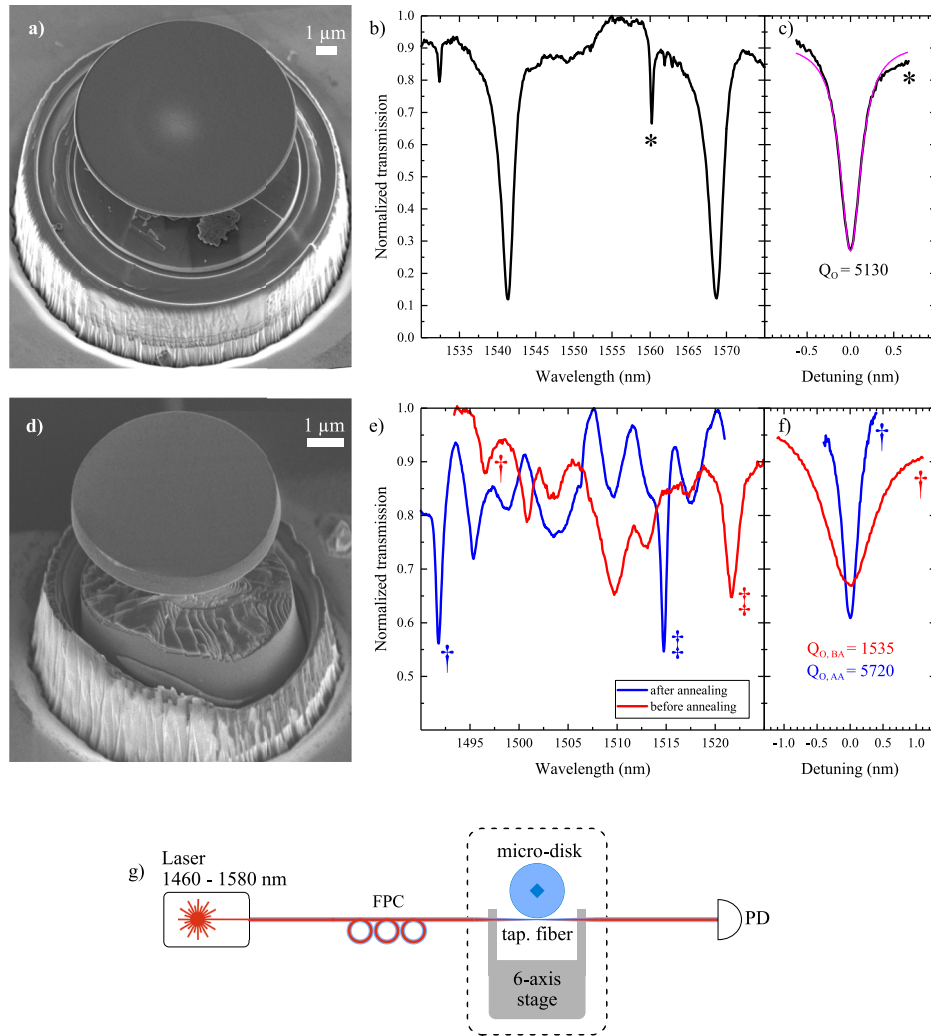


FIG. 3. (a) SEM recording of a diamond micro-disk (diameter $10.5\ \mu\text{m}$, thickness $300\ \text{nm}$) and (b) measured transmission through a tapered fiber probe. (c) High resolution scan of the resonance marked with * in (b). We calculate a quality factor of 5130 by fitting a Lorentzian (purple line) to the measured data (black line). (d) SEM recording of a diamond micro-disk (diameter $5.9\ \mu\text{m}$, thickness $800\ \text{nm}$) and (e) measured transmission before and after $500\ ^\circ\text{C}$ annealing in air for 4 h. The corresponding peaks are marked with † and ‡, showing a blue-shift of $\sim 7\ \text{nm}$ after annealing. (f) High resolution scan of the resonances marked with †. The reported values of the quality factor were extracted as in (c). (g) Scheme of the taper fiber setup used to extract the data in (b), (c), (e), and (f) (FPC: fiber polarization controller, PD: photodetector).

Kawasegi *et al.*, annealing in air at higher temperatures ($600\ ^\circ\text{C}$ and higher) produces roughening of the diamond surface, indicating etching of the diamond phase. At lower temperatures, the surface not exposed to the FIB is not attacked by the thermal annealing, while the exposed area is removed. The resulting structure is shown in Figs. 3(a) and 3(d). To remove the metal layers, we use commercial acid etchants.

III. CHARACTERIZATION AND DISCUSSION

We characterize the micro-disks by measuring the transmission of a tapered fiber probe. The tapered fiber is prepared following the heat-and-draw approach,^{45,46} using a standard SMF-28 telecom fiber. The probe is glued on an aluminum holder, mounted on a 6-axis precision stage, and moved in proximity of the device under test (DUT). The tapered fiber is thin enough at the central part (with diameter on the order of $1\ \mu\text{m}$) to allow coupling the light from a tunable laser into the micro-disk. To measure the optical spectrum and the optical quality factor, we sweep the laser wavelength,

after optimizing the position of the fiber probe and the light polarization [with a fiber polarization controller (FPC)]. A detailed scheme of the measurement setup is shown in Fig. 3(g): the light from a tunable laser (Agilent 81682A) is coupled through the tapered fiber, positioned in proximity of the micro-disk, and the transmission is measured by using a photodetector (PD) (Agilent 81536A). The measurement is performed by scanning the laser wavelength. Light polarization is controlled with a fiber polarization controller, and the position of the fiber is optimized to measure the optical spectrum of a critically coupled micro-disk. Figure 3(b) shows the optical transmission of a tapered fiber in proximity of the micro-disk (diameter 10.5 μm , thickness 300 nm), measured with the setup shown in Fig. 3(g). The free spectral range (FSR) of the cavity is measured as 25 nm, comparable to the value extracted from COMSOL finite element simulations. Only two modes are detected within the FSR, corresponding to the first order radial TE and TM modes. We can assume that the narrower resonances correspond to the TE modes, less sensitive to surface roughness scattering, and the wider resonances correspond to the TM modes. Figure 3(c) shows a higher resolution scan of the resonance peak at 1560 nm. By fitting the measured points to a Lorentzian function, we extract the optical quality factor (Q_O) of 5130.

The overall quality factor can be separated into different contributions,

$$Q_O^{-1} = Q_{SC}^{-1} + Q_{ABS}^{-1} + Q_{BL}^{-1}, \quad (2)$$

where Q_{SC} is the influence of scattering at the sidewalls, Q_{ABS} is the contribution of the absorption, and Q_{BL} is the contribution due to the bending losses. The last term is well in excess of 10^6 for micro-disks of these dimensions, according to COMSOL finite element simulations, and it is not expected to be the limiting contribution of the overall quality factor. Absorption can be caused by impurities present in the diamond substrate before the processing and by implanted gallium during FIB milling. No additional peaks are recorded from confocal Raman spectroscopy of the sample prior to fabrication, indicating negligible amount of impurities of the substrate. It has been previously shown that thermal treatment can be effective in removing the FIB induced damage, i.e., the implanted gallium ions.⁴⁴ We here employ thermal annealing on a micro-disk with diameter 5.9 μm and thickness 800 nm [Fig. 3(d)] to enhance the optical quality factor. Following annealing in air at 500 °C for 4 h, the resonance linewidth is reduced by a factor of 5 (up to a Q-factor value of 5720), and the central wavelength of optical resonances blue-shifted by 7 nm, as highlighted in the measured transmission from the fiber taper probe coupled to the same micro-disk before and after the annealing step in Fig. 3(e). The wavelength shift was measured by comparing the transmission spectra and by identifying the resonance with the same polarization and azimuthal number. We explain the blue-shift with a reduction in the micro-disk size. Considering the resonance condition for a disk resonator,

$$2\pi R_{eff,n} = m\lambda_n / n_{eff,n}, \quad (3)$$

where $R_{eff,n}$ is the effective radius of the optical resonance, m is the azimuthal mode number, λ_n is the resonant wavelength, and $n_{eff,n}$ is the optical mode effective index. Assuming that the effective index change is negligible due to annealing, we can derive the effective radius difference, knowing the central wavelength shift, as

$$\Delta R_{eff} \approx \frac{m\Delta\lambda}{2\pi n_{eff}}. \quad (4)$$

For the measured resonance shift, the radius of the micro-disk is expected to shrink by approximately 15 nm following the annealing. The value is in the same range of the damage depth that can be extracted from the SRIM simulation and is comparable to values reported in the literature.^{26,33,44} The results reported by Kawasegi *et al.*⁴⁴ state that the FIB-irradiated area is selectively etched after thermal annealing. However, from the equation of the resonance condition, the wavelength shift can also be explained by a change in the refractive index. Assuming a constant radius, the change in the effective index is

$$\Delta n_{eff} \approx 2\pi R_{eff} \Delta\lambda / m \approx 0.002. \quad (5)$$

From COMSOL FEM simulations, we can evaluate similar blue shift ($\Delta\lambda_{sim} \approx 6$ nm) of the resonant wavelength by adding a 20 nm layer of a different material with a refractive index of 3 at the outer edge of the micro-disk. Amorphous carbon, graphite, and diamond-like carbon have a higher refractive index than single crystal diamond.^{47–49} Therefore, conversion of non-diamond phase into diamond is

also a possibility. Given the small size variation, it would be challenging to measure the radius change directly (with techniques like atomic force microscopy or by SEM imaging) due to the complex 3D geometry of our structure and the small variation compared to the micro-disk size. It is reasonable to assume that a combination of etching and phase change is the result of the annealing, both contributing to the blue-shift of the resonances. Finally, we verify the presence of elements other than carbon with energy-dispersive X-ray spectroscopy (EDX). The spectroscopy was performed with an X-Max^N module installed in a Zeiss Merlin SEM, using 10 kV electron acceleration voltage to ensure that the emission lines of all the elements of interest are excited. The spectrum was recorded with the field of the SEM centered on the micro-disk. The measurement shows that no foreign elements are present in the volume of the micro-disk [Fig. 4(a)]. Further annealing at 500 °C did not produce any change in the central wavelength or in the linewidth, indicating that any non-diamond phase was fully removed/converted and that the Q-factor is limited by scattering. The additional annealing steps that did not improve further the optical quality were additional 2 h with the same setting and 4 h at 1200 °C in a vacuum (6×10^{-6} mbar).

For this FIB released micro-disk, we identify two main sources of scattering, roughness created by the FIB and roughness by post-release treatments. The undercut process involves aligning rectangular milling patterns to the side of the structure from multiple sample orientations. In this phase, not only precise orientation of the sample but also good control on the ion beam focus and astigmatism is critical to obtain good alignment between the fields. The sputtered metal layer ensures that good focus and astigmatism control is possible, and the optimization of the beam parameters allows better control on the alignment. Lower ion currents correspond to a smaller spot size, thus better resolution, but since diamond is a hard material to etch, a balance must be found between the spot size and etch rate. For the protocol used in this work, we progressively decrease the ion current (and the milling pattern size). Moreover, we alternate the milling direction at each ion current change, enabling the measurement of the angular misalignment and allowing correcting the sample orientation to achieve constant thickness across the micro-disk. We simulate the influence of the misalignment during the

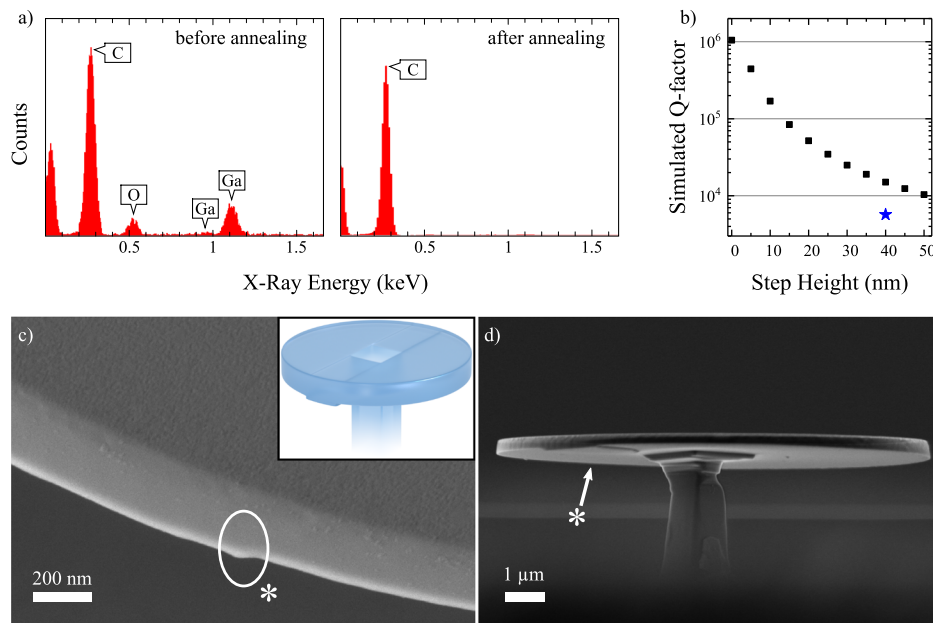


FIG. 4. Energy-dispersive X-ray spectroscopy of the micro-disk before and after the HF cleaning and annealing (a). The recorded spectrum after annealing does not reveal any emission peaks other than carbon, indicating successful removal of Ga⁺ ions. (b) Results from COMSOL simulation to assess the influence of the step on the bottom side: simulated Q-factor with increasing step height (black squares) compared with the measured Q-factor (star). (c) SEM image of the sidewall. The white asterisk marks the step edge caused by the multi-directional milling. For this micro-disk [same as Fig. 3(a)], the step height is about 40 nm. A 3D rendering of the micro-disk with the step edge is shown in the inset. (d) SEM recording of the same micro-disk showing the bottom side.

FIB milling by looking for the eigenmodes of the diamond structure with a COMSOL simulation. We modeled a micro-disk (diameter $5\ \mu\text{m}$, thickness $500\ \text{nm}$) with a square pillar ($1\ \mu\text{m}^2$) and introduced a “step” on the bottom surface, with a step height varying from $0\ \text{nm}$ to $50\ \text{nm}$ [Fig. 4(b)]. For this simulation, 3D geometry was used. We surrounded the diamond disk with an air cylinder with a radius $3\ \mu\text{m}$ bigger than the micro-disk, and we assigned a scattering boundary condition at the air cylinder boundaries to extract the optical quality factor.

If the difference between the micro-disk diameter and the pillar dimension is bigger than $4\ \mu\text{m}$ (i.e., when the pillar is sufficiently far away from the optical mode), we verify that there is no substantial deviation of the simulated optical quality factor between the micro-disk supported by a square section pillar and by a cylindrical one. When we include a step and increase its height, the optical quality factor evaluated by COMSOL degrades from 10^6 for no step to $\sim 10\,000$ for $50\ \text{nm}$ step [Fig. 4(b)]. The height of the step in the fabricated sample is of comparable dimensions [$\sim 40\ \text{nm}$ estimated from SEM measurements, Fig. 4(c)]. Optimization of the FIB milling parameters, or using an ion source capable of smaller beam dimensions, like helium,⁵⁰ will allow to reduce the step height and thus to increase the quality factor; the theoretical resolution of the ion beam of the tool we used is $7\ \text{nm}$, potentially sufficient to reach a value of $Q \sim 100\,000$.

Other source of scattering that limits the overall optical quality factor is smaller scale roughness, visible in Fig. 4(c) on the top surface of the micro-disk. The roughness can be the result of the annealing step performed at $500\ ^\circ\text{C}$. Any instability or deviation of the oven temperature used in the annealing step would accelerate the etch rate of the diamond phase, roughening the surface. Performing annealing at high temperature in a vacuum ($>1000\ ^\circ\text{C}$), similar to the process reported in Ref. 28, followed by HF cleaning to etch the gallium, and finally annealing in air (at $<500\ ^\circ\text{C}$) could help prevent roughening by reducing the temperature at which the diamond surface is exposed in air. The initial annealing in a vacuum will facilitate the diffusion of the implanted Ga^+ ions to the diamond/air interface, but the lack of oxygen will prevent etching of the diamond phase. The following HF cleaning and low temperature annealing will remove the diffused Ga and the non-diamond phase, respectively. The Q-factor scattering component is inversely proportional to the square of the top surface roughness (R_q);⁵¹ therefore, we can expect the quality factor to approach the curve of Fig. 4(b), for the corresponding “step” height. With improved fabrication, we can expect to improve the optical quality factor by 1 order of magnitude, allowing us to reduce the threshold power, required to excite the optomechanical interaction, in the few tens of milliwatt.

IV. CONCLUSIONS

We demonstrate a single crystal diamond micro-disks resonators with an optical quality factor up to 5720 at $1492\ \text{nm}$. The micro-disks were fabricated using a combination of DRIE and FIB milling to create the optical cavity suspended by a square or diamond section support pillar. Thermal annealing in air and HF cleaning proved to be effective to remove FIB induced damage. The effectiveness of the annealing procedure paves the way for reducing optical losses and thus increasing optical Q-factor by up to $5\times$, an important requirement to reduce the threshold power in to excite the mechanical oscillation in optomechanical oscillators.

ACKNOWLEDGMENTS

This research was supported by the Swiss National Science Foundation (Grant No. 157566). Microfabrication was performed at the EPFL Center of MicroNanotechnology. The authors acknowledge the help of Professor Damjanovic at the Group for Ferroelectrics and Functional Oxides, EPFL, for the annealing in a vacuum, the support of Hendrik Schütz at the Laboratory of Photonics and Quantum Measurements, EPFL, with the preparation of the tapered fiber, and the support of the Nanophotonics and Metrology Laboratory at EPFL.

¹ I. Aharonovich, C. Zhou, A. Stacey, J. Orwa, S. Castelletto, D. Simpson, A. D. Greentree, F. Treussart, J.-F. Roch, and S. Praver, *Phys. Rev. B* **79**, 235316 (2009).

² I. Aharonovich, S. Castelletto, D. A. Simpson, C.-H. Su, A. D. Greentree, and S. Praver, *Rep. Prog. Phys.* **74**, 076501 (2011).

- ³ *Cavity Optomechanics*, edited by M. Aspelmeyer, T. J. Kippenberg, and F. Marquardt (Springer Berlin Heidelberg, Berlin, Heidelberg, 2014).
- ⁴ M. Metcalfe, *Appl. Phys. Rev.* **1**, 031105 (2014).
- ⁵ R. Riedinger, A. Wallucks, I. Marinković, C. Löschnauer, M. Aspelmeyer, S. Hong, and S. Gröblacher, *Nature* **556**, 473 (2018).
- ⁶ J. D. Teufel, T. Donner, D. Li, J. W. Harlow, M. S. Allman, K. Cicak, A. J. Sirois, J. D. Whittaker, K. W. Lehnert, and R. W. Simmonds, *Nature* **475**, 359 (2011).
- ⁷ J. Chan, T. P. M. Alegre, A. H. Safavi-Naeini, J. T. Hill, A. Krause, S. Gröblacher, M. Aspelmeyer, and O. Painter, *Nature* **478**, 89 (2011).
- ⁸ D. P. Lake, M. Mitchell, Y. Kamaliddin, and P. E. Barclay, *ACS Photonics* **5**, 782 (2018).
- ⁹ Q. Lin, J. Rosenberg, D. Chang, R. Camacho, M. Eichenfield, K. J. Vahala, and O. Painter, *Nat. Photonics* **4**, 236 (2010).
- ¹⁰ Y. Chu, P. Kharel, W. H. Renninger, L. D. Burkhardt, L. Frunzio, P. T. Rakich, and R. J. Schoelkopf, *Science* **358**, 199 (2017).
- ¹¹ S. Hong, R. Riedinger, I. Marinković, A. Wallucks, S. G. Hofer, R. A. Norte, M. Aspelmeyer, and S. Gröblacher, *Science* **358**, 203 (2017).
- ¹² A. H. Safavi-Naeini, S. Gröblacher, J. T. Hill, J. Chan, M. Aspelmeyer, and O. Painter, *Nature* **500**, 185 (2013).
- ¹³ S. Weis, R. Rivière, S. Deléglise, E. Gavartin, O. Arcizet, A. Schliesser, and T. J. Kippenberg, *Science* **330**, 1520 (2010).
- ¹⁴ W. Yu, W. C. Jiang, Q. Lin, and T. Lu, *Nat. Commun.* **7**, 12311 (2016).
- ¹⁵ A. G. Krause, M. Winger, T. D. Blasius, Q. Lin, and O. Painter, *Nat. Photonics* **6**, 768 (2012).
- ¹⁶ K. Srinivasan, H. Miao, M. T. Rakher, M. Davanço, and V. Aksyuk, *Nano Lett.* **11**, 791 (2011).
- ¹⁷ J. T. Hill, A. H. Safavi-Naeini, J. Chan, and O. Painter, *Nat. Commun.* **3**, 1196 (2012).
- ¹⁸ J. Rosenberg, Q. Lin, and O. Painter, *Nat. Photonics* **3**, 478 (2009).
- ¹⁹ V. Fiore, Y. Yang, M. C. Kuzyk, R. Barbour, L. Tian, and H. Wang, *Phys. Rev. Lett.* **107**, 133601 (2011).
- ²⁰ T. O. Rocheleau, A. J. Grine, K. E. Grutter, R. A. Schneider, N. Quack, M. C. Wu, and C. T.-C. Nguyen, in *2013 IEEE 26th International Conference on Micro Electro Mechanical Systems (MEMS)* (IEEE, 2013), pp. 118–121.
- ²¹ Y. Tao, J. M. Boss, B. A. Moores, and C. L. Degen, *Nat. Commun.* **5**, 3638 (2014).
- ²² X. Sun, X. Zhang, and H. X. Tang, *Appl. Phys. Lett.* **100**, 173116 (2012).
- ²³ W. C. Jiang, X. Lu, J. Zhang, and Q. Lin, *Opt. Express* **20**, 15991 (2012).
- ²⁴ M. Jamali, I. Gerhardt, M. Rezai, K. Frenner, H. Fedder, and J. Wrachtrup, *Rev. Sci. Instrum.* **85**, 123703 (2014).
- ²⁵ J. P. Hadden, J. P. Harrison, A. C. Stanley-Clarke, L. Marseglia, Y.-L. D. Ho, B. R. Patton, J. L. O'Brien, and J. G. Rarity, *Appl. Phys. Lett.* **97**, 241901 (2010).
- ²⁶ I. Bayn, B. Meyler, J. Salzman, and R. Kalish, *New J. Phys.* **13**, 025018 (2011).
- ²⁷ C. F. Wang, Y.-S. Choi, J. C. Lee, E. L. Hu, J. Yang, and J. E. Butler, *Appl. Phys. Lett.* **90**, 081110 (2007).
- ²⁸ J. Riedrich-Möller, L. Kipfstuhl, C. Hepp, E. Neu, C. Pauly, F. Mücklich, A. Baur, M. Wandt, S. Wolff, M. Fischer, S. Gsell, M. Schreck, and C. Becher, *Nat. Nanotechnol.* **7**, 69 (2012).
- ²⁹ L. Li, T. Schröder, E. H. Chen, H. Bakhru, and D. Englund, *Photonics Nanostruct.- Fundam. Appl.* **15**, 130 (2015).
- ³⁰ J. C. Lee, D. O. Bracher, S. Cui, K. Ohno, C. A. McLellan, X. Zhang, P. Andrich, B. Alemán, K. J. Russell, A. P. Magyar, I. Aharonovich, A. Bleszynski Jayich, D. Awschalom, and E. L. Hu, *Appl. Phys. Lett.* **105**, 261101 (2014).
- ³¹ M. J. Burek, Y. Chu, M. S. Z. Liddy, P. Patel, J. Rochman, S. Meesala, W. Hong, Q. Quan, M. D. Lukin, and M. Lončar, *Nat. Commun.* **5**, 5718 (2014).
- ³² M. Mitchell, D. P. Lake, and P. E. Barclay, e-print [arXiv:1808.09883](https://arxiv.org/abs/1808.09883) Cond-Mat Physicsphysics (2018).
- ³³ T. M. Babinec, J. T. Choy, K. J. M. Smith, M. Khan, and M. Lončar, *J. Vac. Sci. Technol., B: Nanotechnol. Microelectron.: Mater., Process., Meas., Phenom.* **29**, 010601 (2011).
- ³⁴ M. J. Burek, N. P. de Leon, B. J. Shields, B. J. M. Hausmann, Y. Chu, Q. Quan, A. S. Zibrov, H. Park, M. D. Lukin, and M. Lončar, *Nano Lett.* **12**, 6084 (2012).
- ³⁵ H. A. Atikian, P. Latawiec, M. J. Burek, Y.-I. Sohn, S. Meesala, N. Gravel, A. B. Kouki, and M. Lončar, *APL Photonics* **2**, 051301 (2017).
- ³⁶ B. Khanaliloo, M. Mitchell, A. C. Hryciw, and P. E. Barclay, *Nano Lett.* **15**, 5131 (2015).
- ³⁷ N. H. Wan, S. Mouradian, and D. Englund, *Appl. Phys. Lett.* **112**, 141102 (2018).
- ³⁸ D. T. Nguyen, C. Baker, W. Hease, S. Sejl, P. Senellart, A. Lemaître, S. Ducci, G. Leo, and I. Favero, *Appl. Phys. Lett.* **103**, 241112 (2013).
- ³⁹ A. Toros, M. Kiss, T. Graziosi, H. Sattari, P. Gallo, and N. Quack, *Microsyst. Nanoeng.* **4**, 12 (2018).
- ⁴⁰ T. Graziosi, S. Mi, M. Kiss, and N. Quack, *Proc. SPIE* **10547**, 105470R (2018).
- ⁴¹ J. F. Ziegler, M. D. Ziegler, and J. P. Biersack, *SRIM: The Stopping and Range of Ions in Matter* (Ion Implantation Press, 2008).
- ⁴² D. P. Adams, M. J. Vasile, T. M. Mayer, and V. C. Hodges, *J. Vac. Sci. Technol., B: Microelectron. Nanometer Struct.* **21**, 2334 (2003).
- ⁴³ I. Bayn, A. Bolker, C. Cytermann, B. Meyler, V. Richter, J. Salzman, and R. Kalish, *Appl. Phys. Lett.* **99**, 183109 (2011).
- ⁴⁴ N. Kawasegi, S. Kuroda, N. Morita, K. Nishimura, M. Yamaguchi, and N. Takano, *Diamond Relat. Mater.* **70**, 159 (2016).
- ⁴⁵ C. Baker and M. Rochette, *Opt. Mater. Express* **1**, 1065 (2011).
- ⁴⁶ R. Rivière, O. Arcizet, A. Schliesser, and T. J. Kippenberg, *Rev. Sci. Instrum.* **84**, 043108 (2013).
- ⁴⁷ S. Xu, B. K. Tay, H. S. Tan, L. Zhong, Y. Q. Tu, S. R. P. Silva, and W. I. Milne, *J. Appl. Phys.* **79**, 7234 (1996).
- ⁴⁸ N. Savvides and B. Window, *J. Vac. Sci. Technol., A* **3**, 2386 (1985).
- ⁴⁹ A. B. Djurišić and E. H. Li, *J. Appl. Phys.* **85**, 7404 (1999).
- ⁵⁰ O. Scholder, K. Jefimovs, I. Shorubalko, C. Hafner, U. Sennhauser, and G.-L. Bona, *Nanotechnology* **24**, 395301 (2013).
- ⁵¹ P. K. Tien, *Appl. Opt.* **10**, 2395 (1971).